Quantitative mapping of key glucose metabolic rates in the human brain using dynamic deuterium magnetic resonance spectroscopic imaging

Xin Li [a], Xiao-Hong Zhu [a,*], Yudu Li [b,c], Tao Wang[a], Guangle Zhang[a], Hannes M. Wiesner[a], Zhi-Pei Liang[b,d] and Wei Chen [a,e,f,*]

[a]Center for Magnetic Resonance Research (CMRR), Department of Radiology, University of Minnesota, 2021 6th St SE, Minneapolis, MN 55455, USA
[b]Beckman Institute for Advanced Science and Technology, University of Illinois at Urbana-Champaign, Urbana, IL 61801, USA
[c]National Center for Supercomputing Applications, University of Illinois at Urbana-Champaign, Urbana, IL 61801, USA
[d]Department of Electrical and Computer Engineering, University of Illinois at Urbana-Champaign, Urbana, IL 61801, USA
[e]Department of Biomedical Engineering, University of Minnesota, Minneapolis, MN 55455, USA
[f]Stem Cell Institute, University of Minnesota, Minneapolis, MN 55455, USA
*To whom correspondence should be addressed: Email: zhuxx022@umn.edu (X.-H.Z.); Email: chenx075@umn.edu (W.C.)
Edited By Christian Metallo

Abstract

Deuterium (^{2}H) magnetic resonance spectroscopic imaging (DMRSI) is a newly developed technology for assessing glucose metabolism by simultaneously measuring deuterium-labeled glucose and its downstream metabolites (1) and has a potential to provide a powerful neurometabolic imaging tool for quantitative studies of cerebral glucose metabolism involving multiple metabolic pathways in the human brain. In this work, we developed a dynamic DMRSI method that combines advanced radiofrequency coil and postprocessing techniques to substantially improve the imaging signal-to-noise ratio for detecting deuterated metabolites and enable robust dynamic DMRSI of the human brain at 7 T with very high resolution (HR; 0.7 cc nominal voxel and 2.5 min/image) and whole-brain coverage. Utilizing this capability, we were able to map and differentiate metabolite contents and dynamics throughout the human brain following oral administration of deuterated glucose. Furthermore, by introducing a sophisticated kinetic model, we demonstrated that three key cerebral metabolic rates of glucose consumption (CMR_{Glc}), lactate production (CMR_{Lac}), and tricarboxylic acid (TCA) cycle (V_{TCA}), as well as the maximum apparent rate of forward glucose transport (T_{max}) can be simultaneously imaged in the human brain through a single dynamic DMRSI measurement. The results clearly show that the glucose transport, neurotransmitter turnover, CMR_{Glc}, and V_{TCA} are significantly higher in gray matter than in white matter in the human brain; and the mean metabolic rates and their ratios measured in this study are consistent with the values reported in the literature. The HR dynamic DMRSI methodology presented herein is of great significance and value for the quantitative assessment of human brain glucose metabolism, aerobic glycolysis, and metabolic reprogramming under physiopathological conditions.

Keywords: cerebral glucose metabolism, aerobic glycolysis, imaging human brain glucose metabolic rates, dynamic DMRSI

Significant Statement

The human brain relies on cerebral glucose metabolism to produce adenosine triphosphate through oxidative and nonoxidative metabolic pathways to support neural activity and brain function. Noninvasive neurometabolic imaging tools are essential for studying glucose metabolism and its changes in the human brain under various pathophysiological conditions. The dynamic ^{2}H magnetic resonance spectroscopic imaging (DMRSI) technology described herein offers unprecedented sensitivity and resolution and enables whole-brain quantitative imaging of three key cerebral metabolic rates in humans, i.e. glucose consumption (CMR_{Glc}), lactate production (CMR_{Lac}), and tricarboxylic acid (TCA) cycle (V_{TCA}), as well as the maximum apparent rate of forward glucose transport (T_{max}), in a single imaging session; thus, it is highly valuable for assessing aerobic glycolysis and metabolic reprogramming in healthy and diseased brains.

Introduction

Glucose is the brain's primary fuel, producing adenosine triphosphate (ATP) via cytoplasmic glycolysis, mitochondrial tricarboxylic acid (TCA) cycle, and oxidative phosphorylation (OXPHOS) to support a variety of cellular activities and brain functions (2–5). In normal brain cells, the TCA cycle and OXPHOS pathways dominate glucose

metabolism (6, 7), whereas in cancer cells, total glucose consumption far exceeds oxidative glucose metabolism, which is known as aerobic glycolysis (AG) or the "Warburg effect" (8–11). Metabolic reprogramming, or elevated AG, occurs not only in cancer cells but is also becoming a central mechanism in healthy and diseased brains. Studies have found that AG plays significant roles in healthy brains

during brain development, neural activation, adaptation learning, and aging process (12–17); and a shift of brain glucose metabolism toward AG has been found in Alzheimer's disease and other neurodegenerative diseases (18–21). However, quantitative assessment of AG and its contribution to human brain glucose metabolism has been challenging due to the lack of neuroimaging tools that can quantitatively measure and image relevant glucose metabolic rates in major pathways. ^{18}F-fluorodeoxyglucose positron emission tomography ([18]FDG-PET) and ^{13}C magnetic resonance (MR) spectroscopic (MRS) imaging (MRSI) or hyperpolarized (HP)-^{13}C-MRS/MRSI techniques are two imaging modalities that can be used to study glucose metabolism in the living brain, but they are not suitable for evaluating AG and metabolic reprogramming (22–29). To determine the extent of AG in various regions of the human brain, Raichle and colleagues measured the brain glucose metabolic rate using [18]FDG-PET and oxygen metabolic rate in the same brain via three separate ^{15}O-PET scans using ^{15}O-labeled water, carbon monoxide, and oxygen, thus, enabling a quantitative study of human brain AG (16, 30–32). Nevertheless, these methods have not been widely used due to their technical challenges or limitations.

Recently, a novel technology based on the in vivo deuterium (^{2}H) MRS (DMRS) or imaging (DMRSI) method combined with an administration of deuterated D-glucose-6,6-d2 (D66) has shown promise in monitoring the dynamics of deuterium-labeled glucose (Glc), the intermediates glutamate and glutamine (Glx: mixed glutamate/glutamine) via the TCA cycle and the glycolytic product lactate (Lac) in the animal and human brains (1, 33–36), and thus, it has the potential to simultaneously assess three key metabolic pathways and associated cerebral metabolic rates of glucose consumption (CMR_{Glc}), TCA cycle (V_{TCA}), and Lac production (CMR_{Lac}). However, due to the low intrinsic sensitivity of deuterium imaging, the low concentration of deuterated metabolites, and the lack of quantification of metabolite contents and metabolic rates, DMRSI technology needs to be further developed to enable quantitative metabolic rate imaging of the human brain with high imaging sensitivity and resolution.

In this work, we designed an optimal proton-deuterium (^{1}H/^{2}H) dual-frequency radiofrequency (RF) whole-head array coil suitable for 7 T ultra-high field (UHF) human brain imaging applications and applied advanced postprocessing methods to further enhance the deuterium signal-to-noise ratio (SNR), thereby greatly improving the DMRSI sensitivity and achieving dynamic DMRSI with high spatiotemporal resolution and whole-brain coverage. We also developed a sophisticated kinetic model and quantification methods for calculating and mapping deuterated metabolite concentrations and three metabolic rates of CMR_{Glc}, CMR_{Lac} and V_{TCA}, as well as the maximum apparent rate of forward glucose transport (T_{max}), from a single dynamic DMRSI measurement. These technological advances have significantly enhanced the capabilities of deuterium metabolic imaging, enabling simultaneous 3D high-resolution (HR) CMR_{Glc}, CMR_{Lac}, and V_{TCA} mapping of the human brain. Utilizing this technology, we studied a group of healthy participants; our preliminary results revealed tissue-specific metabolic activities in the human brain and the relationships among measured metabolic rates and glucose transportation rate.

Results
Advanced RF coil design with optimal performance for whole-brain DMRSI in human at 7 T
The RF coil is a key hardware component of the MRI system, determining the imaging detection sensitivity and SNR, as it acts as an RF power transmitter (Tx) to excite the magnetic resonances of interest and as an RF receiver (Rx) to detect the MR signal. In this study, we aimed to design a multichannel ^{1}H/^{2}H dual-frequency transceiver (Tx/Rx) human head array coil for whole-brain proton and deuterium imaging at 7 T with optimal sensitivity and performance. Since the RF receiver array coil design is a preferred choice to achieve higher SNR and larger imaging coverage (37, 38), and the SNR of the ^{2}H MR signal is proportional to the ^{2}H RF coil reception magnetic field (B_1^-), we performed electromagnetic (EM) simulation to guide RF coil design and determine the appropriate number and size of the ^{2}H head array coils for optimal DMRSI performance at 7 T.

Simulation results show that at 7 T [2]H-operating frequency (45.6 MHz), which is approximately seven times smaller than the 7 T [1]H-operating frequency (297 MHz), increasing the ^{2}H transceiver loop coil size can provide greater B_1^- coverage and better imaging penetration (Fig. S1A). We also simulated the combined ^{2}H RF coil transmission magnetic field (B_1^+) and B_1^- maps of four-, five-, and eight-channel (4ch, 5ch, and 8ch) ^{2}H array coils loaded with a head-shaped water phantom, as well as an eight-element quadrature-driving low-pass birdcage ^{2}H volume coil for comparison (Fig. 1A). The results indicate that the combined B_1^+ and B_1^- field strength distributions from all coil elements showed similar patterns for the array coil configurations, with less uniformity than the birdcage coil (Fig. 1B); more importantly, we found that the B_1^- field ($\propto$SNR) of the 4ch-^{2}H array coil was significantly stronger than all other three coils and was nearly 50% *higher* than that of the 8ch-^{2}H array coil in both peripheral and central regions (Fig. 1C).

Based on the EM simulation results, we designed and fabricated a two-layer ^{1}H/^{2}H dual-frequency transceiver head array coil with passively decoupled 4ch-^{2}H and 4ch-^{1}H array coils. Figure 1D and E displays the schematic design and completed prototype of this head array coil for 7 T human brain imaging applications. The initial coil test using a head-shaped water phantom confirmed that the experimentally measured B_1^+ and B_1^- maps of the 4ch-^{2}H array coil were similar, the measured B_1^+ map was consistent with the simulated B_1^+ field, and a B_1^+ intensity of 0.4 μT/V in the central region and 0.5–0.6 μT/V at the peripheral regions was determined (Fig. S1B). We then collected HR-DMRSI of the natural abundance deuterated water (HDO) and the corresponding T_1-weighted (T_1w) ^{1}H anatomic MRI (Fig. 1F and G) of human brain from a representative healthy participant. High-quality whole-brain DMRSI of tissue deuterium water with high-spatial (0.7 cc nominal voxel size) and temporal (2.5 min per 3D DMRSI volume) resolution was obtained at 7 T. The sensitivity and quality of the 3D HR-DMRSI were evaluated in additional healthy participants, which consistently showed excellent SNR of natural abundance HDO signal in individual DMRSI voxels at the center (SNR = 25.3 ± 2.8) and peripheral (SNR = 26.8 ± 3.4) brain regions (Fig. S2).

Advanced postprocessing approach for further improving the quality of the DMRSI data
Among all detectable deuterated metabolites, the signal of HDO is several times stronger than other metabolites. To reliably detect the deuterated Glc, Glx, and Lac metabolite signals and map their dynamic changes in the human brain, we need to further improve the SNR for HR dynamic deuterium imaging. Previously, we developed an advanced postprocessing method in a rat model based on the Spectral Imaging Exploiting Spatial Spectral Correlations (SPICE) denoising scheme, using a machine learning–assisted subspace model to represent and reconstruct DMRSI signals with
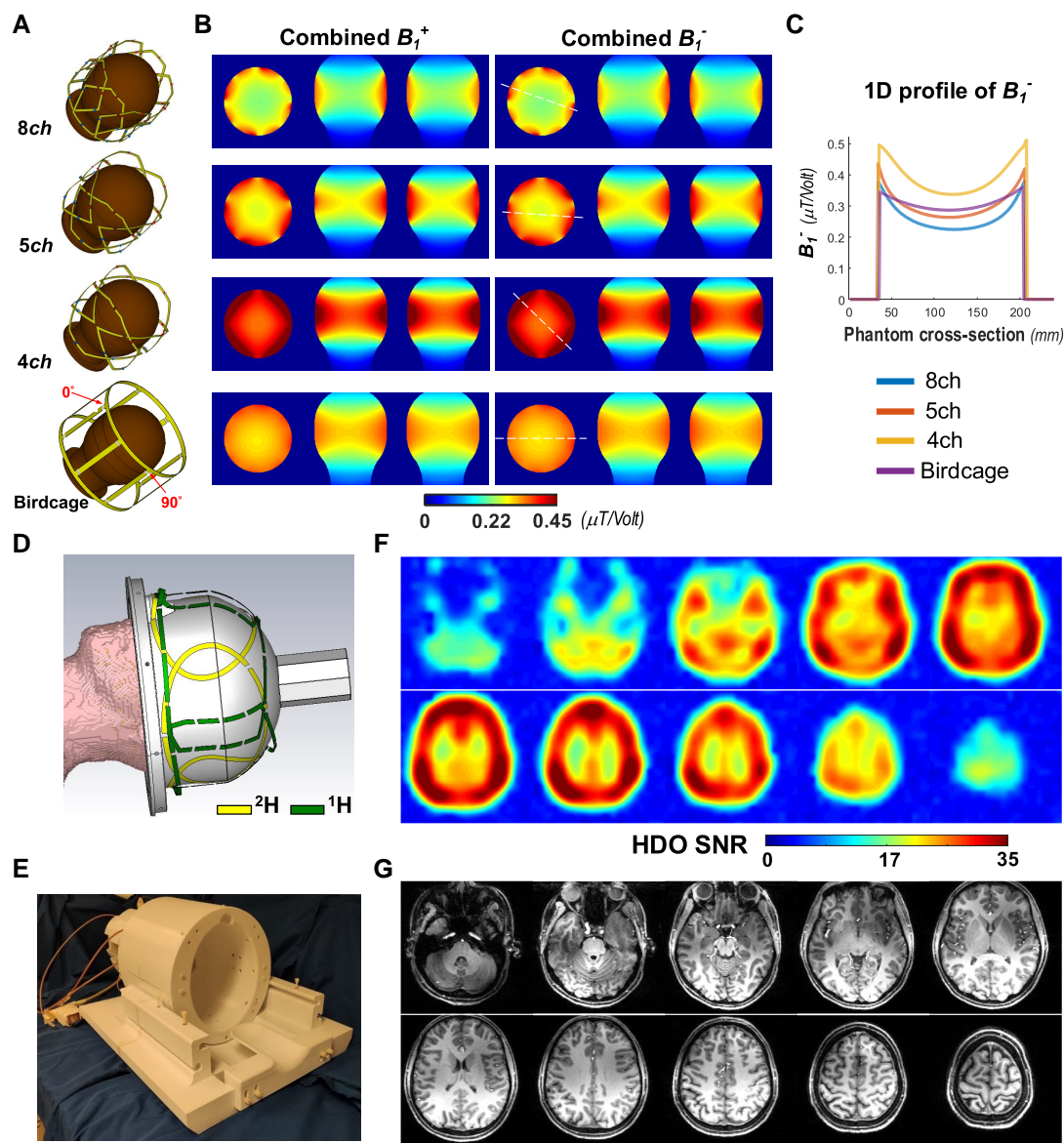
Fig. 1. A) The layout of 4ch, 5ch, and 8ch ^2H RF transceiver array coils and a quadrature-driving low-pass birdcage ^2H volume coil loaded with a head-shaped water phantom operating at 45.6 MHz; B) EM simulated combined B_1^+ (left) and B_1^- (right) maps of these coils shown in three orientations; and C) 1D profiles of the B_1^- fields across the middle of the phantom (see dashed lines in B). D) The schematic design and E) the prototype of a 4ch $^1H/^2H$ dual-frequency transceiver array coil for 7 T human brain imaging study. F) HR whole-brain deuterium natural abundance water (HDO) SNR maps with 0.7 cc nominal voxel and 2.5 min acquisition, and G) the corresponding T_1w ^1H anatomical MRI obtained from a representative healthy subject using the coil shown in (E).

several times improvement in SNR (39–41). This SPICE-based processing method was further optimized for human brain DMRSI applications (see the details about SPICE method in Supplementary Material), and its effect on sensitivity enhancement was carefully evaluated in this study.

Figure 2 shows a typical slice of SPICE-processed 3D DMRSI data in a healthy brain (Fig. 2A); representative original and SPICE-processed ^2H spectra and stack plots of SPICE-denoised dynamic spectra in gray matter (GM) voxel (Fig. 2B) and white matter (WM) voxel (Fig. 2C), respectively, after D66 oral administration; as well as multislice ^1H MRI and corresponding SNR maps of HDO, Glc, Glx, and Lac/lipid metabolite signals 2 h after D66 intake (Fig. 2D), where the dynamic 3D DMRSI data was acquired with 2.5 min temporal resolution. To evaluate the effect of the SPICE approach and compare the quality and sensitivity of the ^2H spectra and metabolite SNR maps, the single-frame original,

four-frame-averaged original, and single-frame SPICE-processed data are presented side by side. As expected, the four-frame-averaged original spectra were *two times* less noisy than the original spectra, and the single-frame SPICE-processed spectra further reduced spectral noise while capturing the metabolite signals, so that the HDO, Glc, and Glx and Lac signals (with chemical shifts of 4.8, 3.8, 2.4, and 1.2 ppm, respectively) were clearly identified, and spectral differences between the GM and WM voxels were observed. Specifically, we found that the SPICE-denoised single-frame DMRSI data showed a *2- to 3-fold* SNR improvement for all four metabolites over the original single-frame data, and ~1.5-fold SNR improvement compared with the four-frame-averaged original data. The large SNR enhancement significantly improves the quality of the metabolite maps, especially for low-level metabolites, such as Lac. It is worth noting that the detected Lac signal in the cortical regions close to the skull/skin with abundant lipids may contain lipid
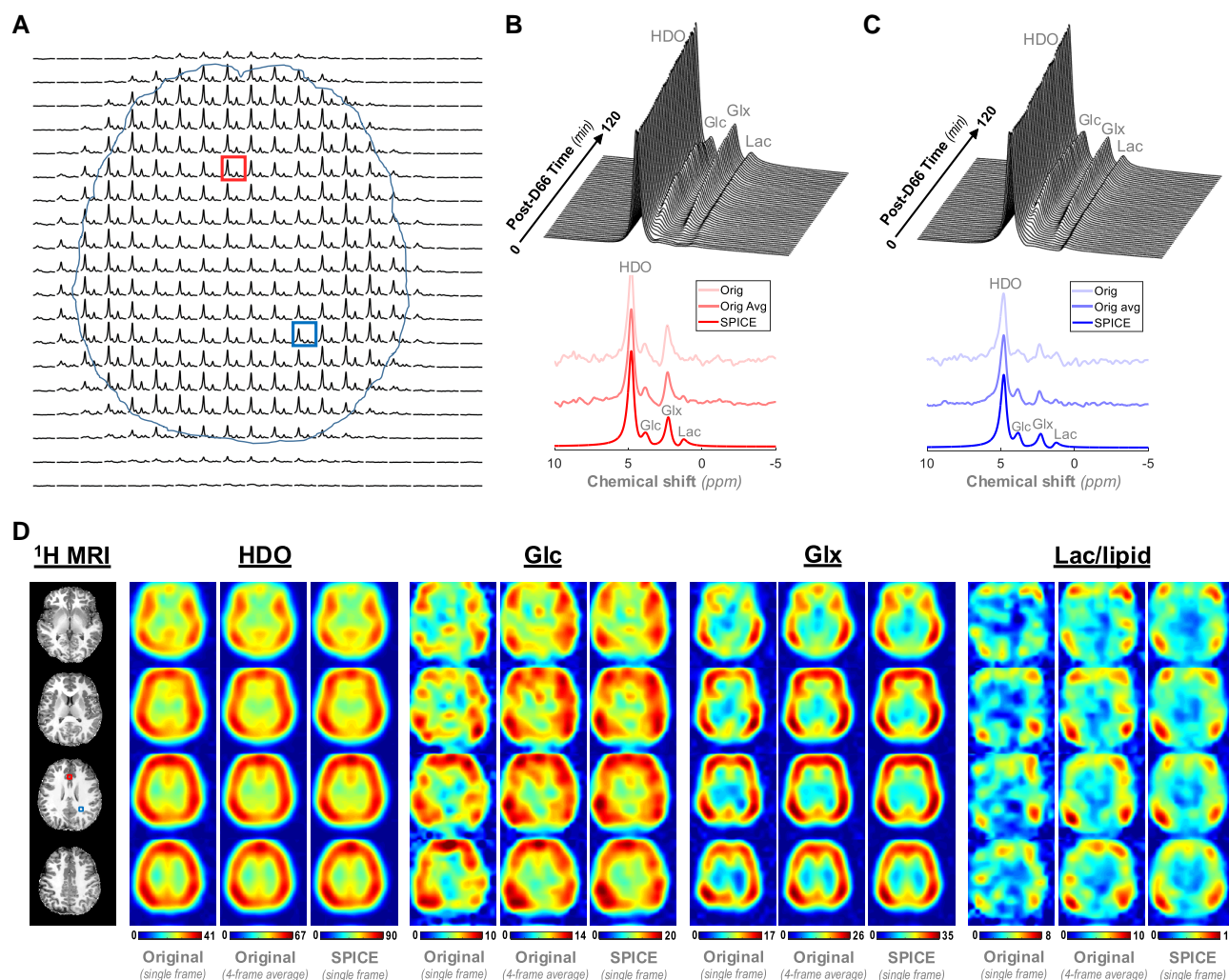
Fig. 2. A) A representative slice of 3D DMRSI data from a healthy brain with SPICE-based postprocessing. The ^{2}H spectra before (original) and after SPICE processing were obtained from B) a GM voxel and C) a WM voxel acquired 120 min post-D66 administration, as well as the corresponding stack plots of SPICE-processed dynamic ^{2}H spectra with 2.5 min temporal resolution. D) Four axial slices of ^{1}H MRI and the corresponding DMRSI SNR maps of brain HDO, Glc, Glx, and Lac/lipid metabolite signals obtained 2 h after oral D66 glucose administration. The single-frame original data (left column) was acquired with 0.7 cc nominal voxel size and 2.5 min per 3D DMRSI volume, the original with four-frame average (i.e. 10 min scan, middle column) and single-frame SPICE-processed (right column) DMRSI data are displayed for comparison.

signals since their chemical shifts are almost the same. We removed the skull in subsequent data analysis to reduce lipid contamination.

SPICE-based processing approach also largely reduced the temporal fluctuation of metabolite signals across multiple 3D DMRSI volumes. The coefficient variation (CV) of natural abundance brain HDO signals in three representative participants was evaluated to compare temporal variation in original data (CV$_{Original}$ = $4.9 \pm 3.0\%$, $6.1 \pm 4.6\%$, and $5.5 \pm 3.9\%$) and SPICE-processed data (CV$_{SPICE}$ = $0.5 \pm 0.3\%$, $1.0 \pm 0.5\%$, and $0.5 \pm 0.3\%$), where an *8- to 10-fold* reduction in CV was observed in the SPICE-processed data. Figure 3 presents multislice Glx molar concentration ([Glx]) maps derived from single-frame original (Fig. 3A), four-frame-averaged original (Fig. 3B) and single-frame SPICE-processed (Fig. 3C) data at different time points after oral D66 intake; the corresponding concentration time courses of HDO, Glx, Glc, and Lac in representative WM (Fig. 3D) and GM voxels (Fig. 3E) are also shown. Again, the quality of the [Glx] map derived from the single-frame SPICE-processed data was better than that of the four-frame-averaged original data, which in turn was

much better than the single-frame original data. Furthermore, Fig. 3D and E clearly show that the temporal fluctuation of all metabolites was greatly reduced after SPICE denoizing; although the four-frame moving average can also reduce the temporal fluctuation of the original date, the reduction was smaller than that of SPICE denoizing.

Quantitative mapping of metabolite concentrations and dynamics in the human brain

The metabolite maps and dynamics shown in Fig. 3 were expressed in millimolar (mM) concentrations. To convert ^{2}H metabolite signals to molar concentrations, we developed a quantification method that corrects for magnetization saturation factors (SFs) and brain tissue water fraction. Details of the method are described in the Materials and methods section; Fig. S3 shows an example of quantifying different metabolite concentrations to generate pre- and postcorrection maps. The corrected metabolite concentration maps (Fig. S3C) appear more uniform and represent the true metabolite contents in the human brain.
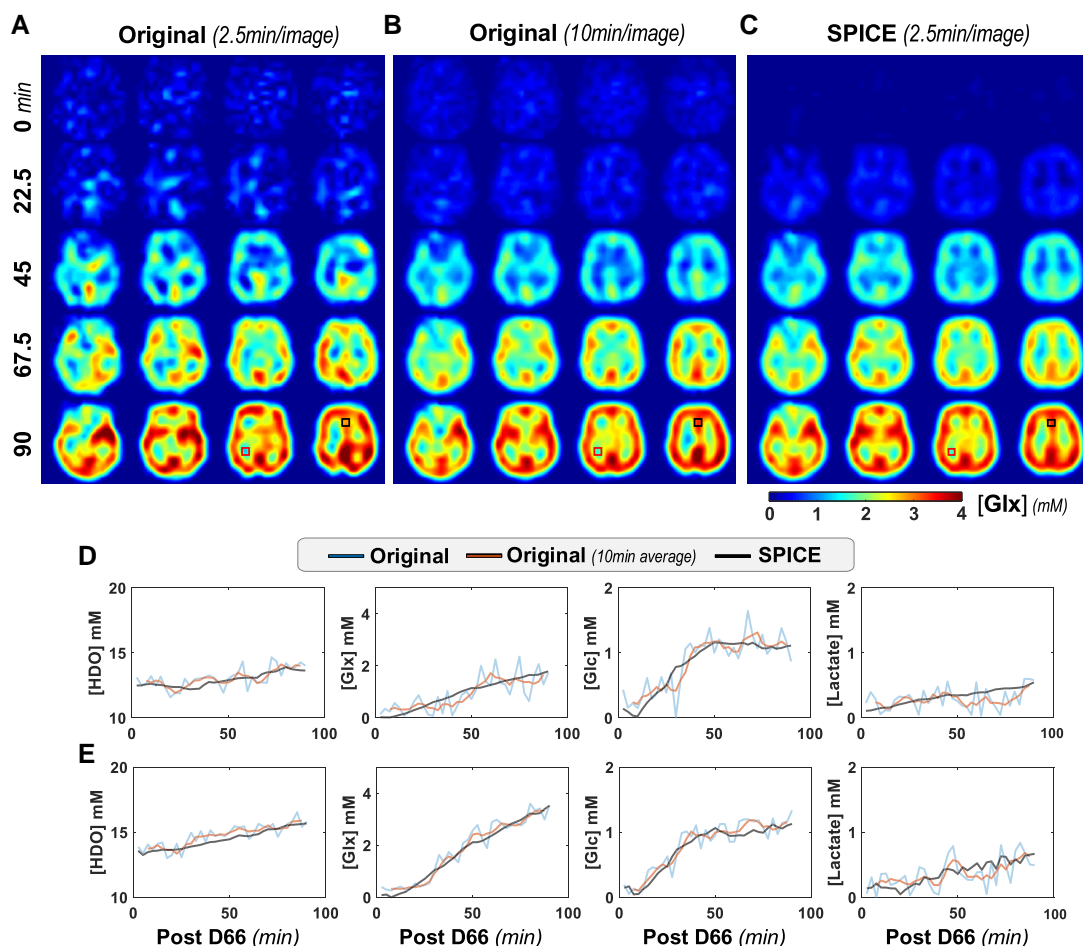
Fig. 3. Four axial slices of brain Glx concentration maps derived from A) single-frame original data, B) 10 min (four frames) averaged original data, and C) single-frame SPICE-processed data at 0, 22.5, 45, 67.5, and 90 min post-D66 administration. The original, 10-min time-moving-averaged original and SPICE-processed time courses of HDO, Glx, Glc, and Lac concentrations in representative WM and GM voxels (marked in A–C) are shown in (D) and (E), respectively.

Figure S4A and C present two examples of whole-brain dynamic metabolite concentration maps (in three orientations) of HDO, Glc, Glx, and Lac at 22.5, 45, 67.5, and 90 min after D66 ingestion from two representative subjects; Fig. S4B and D show the corresponding time courses of the metabolites in brain regions dominated by WM (WM ≥ 60%) and GM (GM ≥ 55%), respectively. As expected, the concentration of deuterated metabolites increased over time after D66 administration, and different metabolites or tissue types show different dynamics or contrast. In particular, we found that the [Glx] of the GM increased faster and reached a higher level than that of the WM. Movies S1 and S2 are examples of whole-brain Glx concentration maps obtained 120 min after oral D66 administration (Movie S1), and a representative slice of dynamic Glx concentration images of the same brain during post-D66 period (Movie S2), where high quality and clear GM-WM contrast of [Glx] imaging can be appreciated.

Figure S5 exhibits the dynamics of deuterated metabolites in GM- and WM-dominated brain voxels obtained in other participants, where Fig. S5A–D shows the result of two individuals, each undergoing two measurements on different days. In all subjects, we consistently observed a faster upward trend in [Glx] for GM than for WM, and the [Glx] gradually approached a stable level about 90–120 min post-D66. Subsequently, we performed regression analysis using 90-min post-D66 DMRSI data from multiple

subjects to determine Glx concentrations in different brain tissue types. One brain MRI slice containing both GM and WM tissues was selected from each subject (Fig. S6A), and GM fraction (F_{GM}) maps were generated from brain structural images and matched to DMRSI resolution (Fig. S6B). Corresponding [Glx] maps for each subject were derived from 10-min-averaged original (Fig. S6C) and 2.5-min SPICE-processed (Fig. S6D) DMRSI data, respectively. Regression analysis between [Glx] and GM fraction indicated that the slopes and intercepts of brain Glx concentration for Original_10min (Fig. S6E) and SPICE_2.5min (Fig. S6F) DMRSI data were consistent across different subjects, revealing a mean [Glx] of 3.9 ± 0.4 and 4.0 ± 0.2 mM in pure GM, and 1.2 ± 0.2 and 1.4 ± 0.3 mM in pure WM ($n = 5$), respectively. Thus, the amount of deuterated Glx produced by D66 metabolism in pure GM is ~3-fold higher than in pure WM, resulting in an excellent [Glx] contrast between human brain GM and WM tissues.

We also evaluated the reproducibility of repeated dynamic DMRSI, where the experimental procedure, setup, and acquisition parameters remained identical for both measurements on the same brain. High similarities were observed in the concentration dynamics of each metabolite in the same tissue type (Fig. S5A–D), and in [Glx] images of the same brain slice from two independent measurements (Fig. S7A and C) of two individuals. Figure S7B and D present the correlation analysis results of voxel-based

dynamic [Glx] data acquired 0–90 min (first participant) and 0–68 min (second participant) after D66 ingestion, which revealed the following relationship: $y = 0.74x + 0.03$ ($R^2 = 0.91$, $P < 0.005$) and $y = 0.95x - 0.20$ ($R^2 = 0.88$, $P < 0.005$) for the repeated scans in these two participants. Overall, the metabolic activity measured in the same brain was highly reproducible, although the first participant was found to have lower [Glx] in the second scan, possibly due to insufficient waiting time between the two scans, so the deuterium water label introduced in the first scan had not yet been completely cleared from the body before the second scan, resulting in an underestimation of [Glx] levels in the second scan.

Simultaneous whole-brain metabolic rate imaging of CMR_{Glc}, CMR_{Lac}, and V_{TCA} in humans

With the ability to map the deuterated metabolite concentrations and dynamics, we introduced a sophisticated kinetic model to quantify the three cerebral glucose metabolic rates of CMR_{Glc}, CMR_{Lac}, and V_{TCA} in the human brain based on the Glc, Glx, and Lac concentration time courses, and the blood glucose input functions obtained from the arterialized venous blood sampling. The workflow for whole-brain metabolic rate imaging is shown in Fig. 4A, and the kinetic model is illustrated in Fig. 4B. Details of the kinetic model and relevant model parameters are described in the Materials and methods section, while examples of blood input functions of total and ^{2}H-labeled glucose, as well as model fittings of multiple metabolite time courses in a representative brain DMRSI voxel, are illustrated in Fig. 4A.

Using the kinetic model, we obtained whole-brain metabolic rate maps of CMR_{Glc}, V_{TCA}, and CMR_{Lac} from healthy volunteers. Figure 5A shows multislice ^{1}H MRI of brain structure, GM fraction map, and the corresponding images of CMR_{Glc}, V_{TCA}, and CMR_{Lac}, as well as T_{max}, derived from the kinetic model in a representative participant. Similar metabolic rate maps of the other four participants are presented in Fig. S8. The tissue contrast found in the CMR_{Glc} and V_{TCA} maps appeared to be similar to the GM fraction maps, with higher CMR_{Glc} and V_{TCA} in the GM consistently observed across all participants. As shown in Fig. 5B, we performed linear regression analyses of CMR_{Glc}, CMR_{Lac}, and V_{TCA} versus F_{GM} for each brain using the data from all DMRSI voxels within the brain slices. The intercepts of the F_{GM} at 0 and 1 (i.e. 100%) represent the estimated metabolic rates of pure WM and pure GM, respectively. We found that CMR_{Glc} was ~2.5 *times* higher and V_{TCA} was *about 1.7 times* higher in pure GM than in pure WM, indicating higher metabolic activity and energy budget in GM (42). Interestingly, a similar contrast was found in T_{max}, indicating a higher glucose transport influx in GM than WM (Fig. 5).

Table 1 summarizes the values of CMR_{Glc}, CMR_{Lac}, V_{TCA}, and T_{max} in pure GM, pure WM, and whole-brain-average for all five participants. The resulting mean values of CMR_{Glc} in GM, WM, and whole brain are consistent with literature reports of the human brain PET and ^{1}H MRS measurements (25, 43–45). Furthermore, we analyzed the correlation of individual participants' CMR_{Glc}, V_{TCA}, CMR_{Lac}, and T_{max} values of pure GM; the results are summarized in Fig. 6, showing a strong linear correlation between the metabolic rates of CMR_{Glc} and V_{TCA} (Fig. 6A), CMR_{Glc} and CMR_{Lac} (Fig. 6B); and the relationship between the glucose transportation rate T_{max} and CMR_{Glc} (Fig. 6C), as well as between T_{max} and V_{TCA} (Fig. 6D). We found that the ratio of V_{TCA} to CMR_{Glc} was 1.7, and the percentage of glucose used in AG (i.e. $CMR_{Lac}/[2 \times CMR_{Glc}]$) in the resting healthy brain was ~16%. In addition, the ratios of T_{max}/CMR_{Glc} were 4.6 in pure WM, 3.8 in pure GM, and 4.1 in whole brain (Table 1), respectively; the determined T_{max} values agreed well with a single-voxel localized ^{1}H MRS human brain study (43).

Discussion

Interest in ^{2}H MRS–based metabolic imaging technology and applications has grown rapidly in recent years because this novel imaging method can be used to noninvasively map cellular metabolism after introducing deuterium-labeled substrates, and it is technically simple and robust compared with other MR-based metabolic imaging techniques (46–50). In addition to monitoring glucose uptake like FDG-PET, DMRSI can also detect deuterated downstream metabolites; in particular, deuterated Lac is associated with the AG pathway and deuterated Glx is associated with oxidative TCA cycle activity (1, 46, 47, 50). Currently, the promise of deuterium metabolic imaging is mainly demonstrated in oncology for the detection of the "Warburg Effect" in tumors with excellent imaging contrast, where only steady-state or low-resolution dynamic imaging is used (33, 40, 46, 51–58). The major technical challenges are the inherent low deuterium sensitivity and low concentrations of deuterated metabolites, resulting in poor SNR and imaging resolution, limiting the potential of ^{2}H MRS–based metabolic imaging for broad biomedical applications and translation.

Dynamic DMRSI has the potential to simultaneously map the three metabolic rates of CMR_{Glc}, V_{TCA}, and CMR_{Lac} in the human brain, which is of great significance for studying AG and/or metabolic reprogramming under various brain conditions and cannot be achieved by other imaging techniques alone. However, dynamic DMRSI requires even higher sensitivity than steady-state deuterium imaging, as signal averaging is only allowed over a limited time to achieve sufficient SNR and spatiotemporal resolution to capture the dynamic changes of deuterated metabolites. Therefore, to realize the full potential of this novel neurometabolic imaging technology, it is essential to improve the sensitivity and capabilities of the DMRSI technique.

Our first goal is to develop an optimized RF head array coil for whole-brain deuterium imaging in humans at 7 T. Through EM simulations, we found that at low RF coil operating frequency, the 4ch-^{2}H head array coil with larger size coil elements covering the entire human head can provide significantly better performance in both central and peripheral brain regions than commonly used ^{2}H birdcage volume and 8ch ^{2}H head array coils (34, 59) because the coverage and penetration of low-frequency B_1 field largely depend on RF coil size (Fig. S1A). Our prototype 4ch-^{2}H head array coil had four large loop elements and provided excellent decoupling through well-designed geometric overlap and modified resonant inductive decoupling (RID) circuits (60, 61). The experimentally measured B_1^+ field of this coil agreed well with the simulation results (Fig. S1B) with 0.4 and 0.5–0.6 µT/V in the central and peripheral regions, respectively, which is *two to three times* stronger than that of 8ch-^{2}H head array coils reported in 7 and 9.4 T studies (34, 59). Using this coil, we acquired human whole-brain DMRSI data with *0.7 cc* nominal voxel and *2.5 min* per volume resolution, and achieved SNR > 25 in most brain regions for the natural abundance water (HDO) signals *without* applying SPICE denoizing (Figs. 1F and S2). Compared with a similar 9.4 T human brain study using an 8ch-^{2}H head array coil (34), we achieved *2–4.6 times* higher SNR and ~4-*fold* better spatial and temporal resolution in *original* DMRSI data collected at 7 T. Therefore, the 4ch-^{2}H head array coil offers a simpler, more cost-effective RF coil solution with superior performance, which is
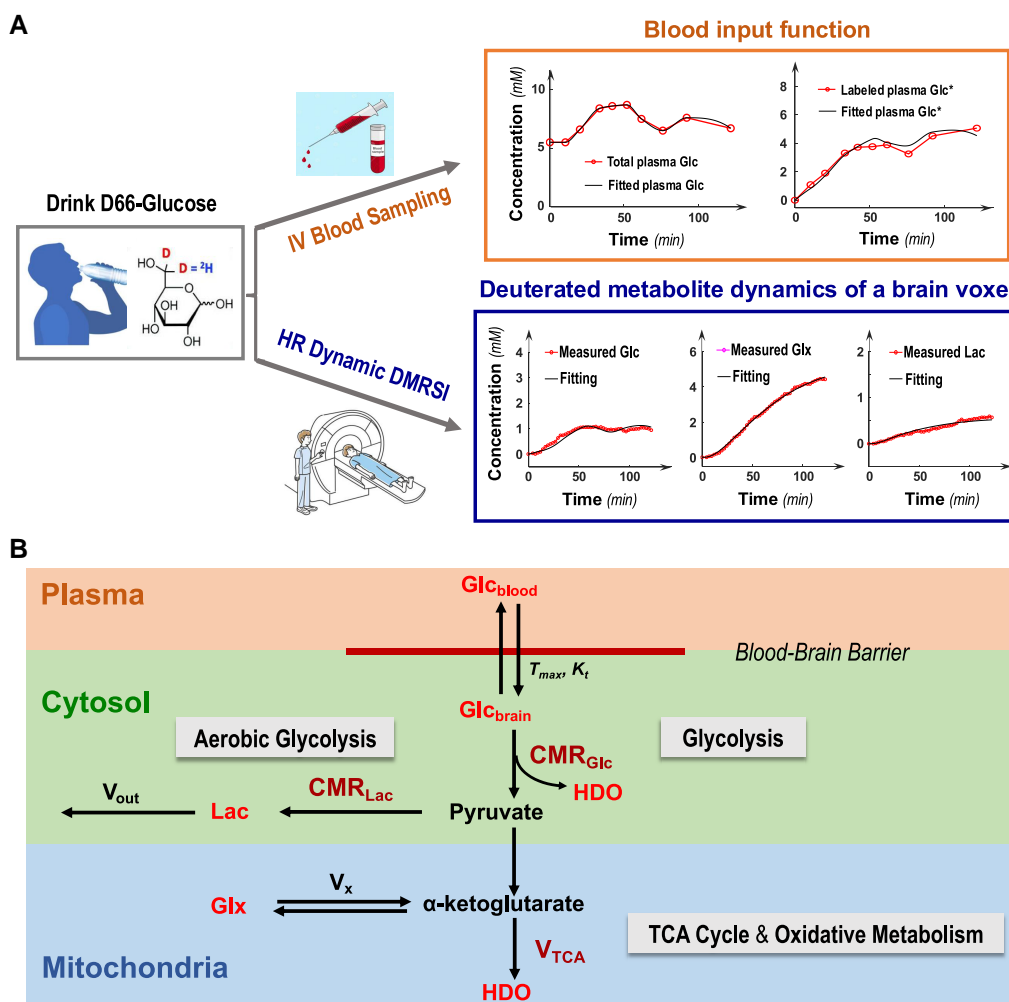
Fig. 4. A) Whole-brain metabolic rate imaging workflow based on the dynamic DMRSI measurement. Following the drink of labeled glucose (D66) solution, HR dynamic DMRSI acquisition is conducted together with the blood glucose input functions measurement through IV blood sampling. Examples of measured and fitted blood glucose input functions, and the corresponding deuterated metabolite dynamics and kinetic model fitting of a representative brain voxel are demonstrated. B) A metabolic kinetic model developed for quantifying cerebral glucose metabolic rates of CMR_{Glc}, CMR_{Lac}, and V_{TCA}, as well as maximal glucose transport rate of T_{max} in each brain imaging voxel using the corresponding deuterated metabolite concentration time courses and the blood glucose input functions as illustrated in (A).

critical for imaging the dynamics of deuterated metabolites in the human brain.

By applying SPICE-processing methods (40), we greatly reduced the ^{2}H spectral noise and temporal fluctuations of dynamic deuterated metabolite signals, further improved imaging sensitivity and reliability, and enabled dynamic DMRSI of the entire human brain to reach the highest spatiotemporal resolution to date. Our results show that >2-fold SNR gain can be realized for dynamic DMRSI, and an 8- to 10-fold reduction in the coefficient of variation was observed in the natural abundance human brain HDO signal after SPICE denoizing. Such improvements can be translated into higher resolution, better quality, and more reliable deuterium metabolic imaging data. Lac had particularly benefited from SPICE processing, as Lac signal and its dynamic changes were better identified and tracked on a voxel-by-voxel basis, and the quality of the Lac maps was significantly improved (Figs. 2 and S4). After SPICE processing, the temporal fluctuations of *all* deuterated metabolites were minimized (Fig. 3D and E), providing more reliable regression results for analyzing dynamic DMRSI data using the kinetic model fitting.

Most literature work rarely reports metabolite concentrations or metabolic rates because converting ^{2}H metabolite signal into molar concentration is not straightforward, and quantifying metabolic rate is more difficult and requires an appropriate kinetic modeling. However, it is desirable to obtain metabolic information in absolute units to be able to assess and direct compare the metabolic status of the human brain at different scanning sites, times, and/or physiopathological conditions (62). Therefore, we developed a novel quantification method and kinetic model to calculate the concentrations of deuterated Glc, Glx, and Lac, and derive the metabolic rates of CMR_{Glc}, CMR_{Lac}, and V_{TCA} for all DMRSI voxels within the human brain. In this process, the magnetization saturation factor (SF) for different metabolites (due to the short repetition time used), inhomogeneous B_1^+ field distribution of the RF coil (i.e. RF pulse flip angle (FA) map), and the tissue water content in different imaging voxels were all accounted for and/or corrected (Fig. S3). Such correction is necessary for generating reliable and accurate metabolite concentration maps and time courses. To calculate metabolic rates based on the metabolite concentration dynamics, we developed a kinetic model that was modified from our previous model (1) to include the AG pathway (Fig. 4B); measurements of total and deuterated blood glucose changes were also required as the blood
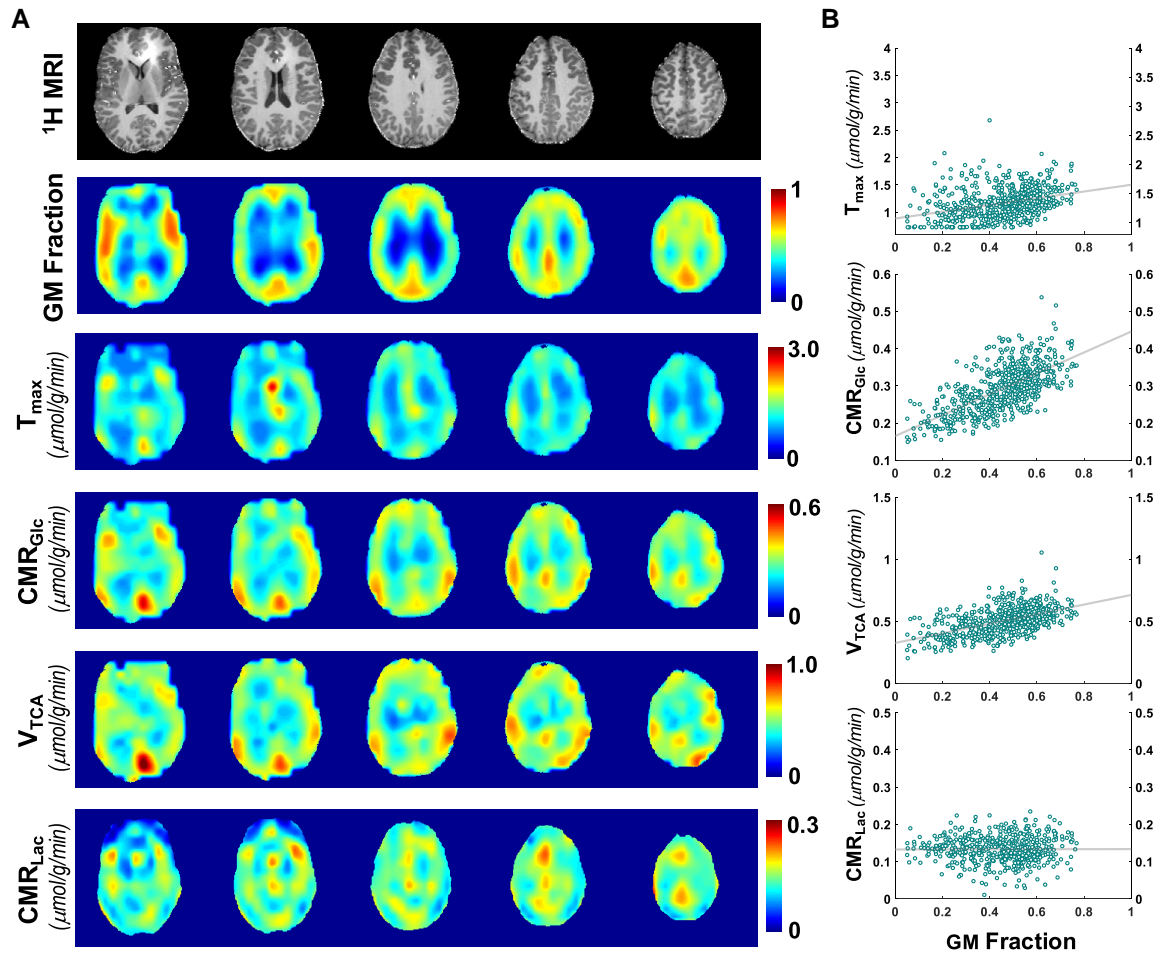
Fig. 5. A) Multislice ^{1}H MRI of brain structure, GM fraction, and the corresponding T_{max}, CMR_{Glc}, V_{TCA}, and CMR_{Lac} maps in the axial orientation derived from the kinetic model in a representative subject (participant 1) are presented. B) Linear regression of T_{max}, CMR_{Glc}, V_{TCA}, and CMR_{Lac} as a function of GM fraction, with the intercepts at GM fraction of 0 and 1 representing the values in the pure WM and pure GM, respectively. The regression results from this subject, along with the results from four other healthy participants, are summarized in Table 1.

input functions. The model fitted the Glc, Glx, and Lac concentration time courses very well (Fig. 4A), yielding whole-brain metabolic rate maps of CMR_{Glc}, CMR_{Lac}, and V_{TCA} in a group of healthy participants (Figs. 5 and S8).

With the substantial improvement of DMRSI technical capabilities, we have obtained high-quality whole-brain dynamic DMRSI data at 7 T, achieving the highest spatiotemporal resolution of human brain deuterium imaging reported so far; and enabled simultaneous imaging of glucose transportation rate constant and three key glucose metabolic rates covering both oxidative and nonoxidative pathways with a single dynamic HR-DMRSI measurement. Our results reveal the following interesting findings.

First, we found that the dynamic DMRSI measurements were highly reproducible with consistent metabolic dynamics. Voxel-based (Fig. 3D and E) and ROI-based (Figs. S4 and S5) time courses revealed detailed metabolic dynamic features, such as rapid Glx and Glc turnovers and relatively slow HDO evolutions, which provide a solid basis for characterizing glucose metabolic activity in various brain regions and enable reliable kinetic modeling.

Second, we observed clear GM–WM contrast in all [Glx] maps, and in T_{max}, CMR_{Glc}, and V_{TCA} maps of all participants studied.

Linear regression analyses showed that the deuterated Glx content in pure GM was about *3 times* higher than that in pure WM (Fig. S6); at the same time, T_{max}, CMR_{Glc}, and V_{TCA} in pure GM were *2.0*, *2.5*, and *1.7 times higher*, respectively (Table 1). These results indicate that the glucose transport and utilization and TCA cycle activity are much higher in GM to support intense neuronal activity and high ATP energy demand. They are consistent with literature findings, in which ^{18}FDG-PET studies reported that glucose consumption rate of GM was 2–3 times higher (25, 44); ^{13}C-MRS studies reported that the TCA cycle activity rate of GM was 68% higher (63, 64); and a ^{31}P-MRSI study reported that the ATP synthesis rate of GM was 3-fold higher (65). The overall results of T_{max} values and T_{max}/CMR_{Glc} ratios, and their GM–WM differences obtained in this work (Figs. 5 and 6 and Table 1) also agreed with the previous single voxel ^{1}H MRS study (43) and the neurochemistry underlying brain glucose transportation and metabolism, thus supporting the use of advanced DMRSI and kinetic model for quantitative whole-brain mapping of key glucose metabolic and transportation rates in the human brain.

Third, based on the simultaneously measured metabolic rates, we were able to assess the contributions of aerobic and oxidative glycolysis in the same brain or brain tissue type by determining the ratios of different metabolic rates. For instance, we found
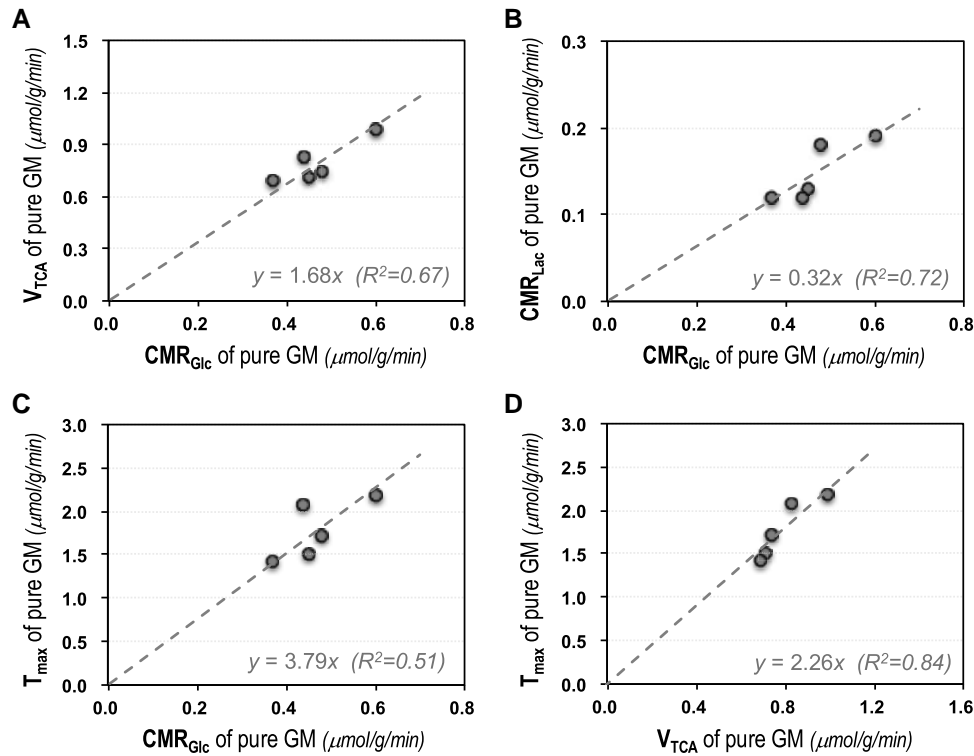
Fig. 6. Regression analysis of individual participants' CMR_{Glc}, V_{TCA}, CMR_{Lac}, and T_{max} values in pure GM as listed in Table 1: A) correlation between the metabolic rates of CMR_{Glc} and V_{TCA}, and B) between CMR_{Glc} and CMR_{Lac}, C) correlation between the glucose transportation rate T_{max} and the corresponding metabolic rate of CMR_{Glc}, and D) between T_{max} and V_{TCA}. Their linear relationships and the correlation coefficients are shown in each plot with statistical significance ($P < 0.005$).

that the whole-brain V_{TCA} to CMR_{Glc} ratio is ~2; the whole-brain AG contribution (i.e. $CMR_{Lac}/[2 \times CMR_{Glc}]$) is around 20%, which is ~2 times higher in pure WM than in pure GM (Table 1); regional specific AG contribution in individual brains can also be quantified from their CMR_{LAC} and CMR_{Glc} maps. Furthermore, we found statistically significant positive correlations between CMR_{Glc} and V_{TCA}, and between CMR_{Glc} and CMR_{LAC} in pure GM of individual brains; significant positive correlations were also found between the maximal glucose transport rate (T_{max}) and the metabolic rates of CMR_{Glc} and/or V_{TCA} in pure GM (Fig. 6). Even using state-of-the-art neuroimaging techniques, assessing these relationships in the human brain is difficult, if not impossible.

As the metabolic reprogramming between the nonoxidative and oxidative glucose metabolism plays an essential role in healthy and diseased brains, the quantitative dynamic DMRSI technology described herein is the only neuroimaging modality capable of noninvasively and simultaneously mapping key glucose metabolic rates along the oxidative and nonoxidative pathways with whole-brain coverage and superior sensitivity and resolution; therefore, it provides an essential neurometabolic imaging tool for quantitative investigation of neuroenergetics and glucose metabolic reprogramming associated with normal brain function and dysfunction.

The current study was conducted on a 7 T human scanner, which is the highest field strength FDA approved for clinical use. We can benefit from the UHF scanner as it significantly improves the sensitivity and spectral resolution of ^{2}H MRS imaging (66). Nonetheless, the DMRSI technology developed at UHF can be easily adapted at lower field, such as 3 T; several exploratory studies have already been published to demonstrate the feasibility

(67, 68). Compared with similar studies conducted at UHF, it is expected that the spatial and temporal resolution of low-field DMRSI will be sacrificed due to loss of sensitivity. However, the optimal RF coil design, the SPICE-processing method, and the kinetic model as described in this work can be applicable and beneficial for 3 T human brain DMRSI applications.

In this work, we focused on establishing an HR dynamic DMRSI technique for quantitative whole-brain mapping of key glucose metabolic rates with oral D66-glucose administration, which is more practical than intravenous infusion in human applications. Compared with steady-state deuterium imaging, longer acquisition is required for dynamic DMRSI to capture the slow metabolic process of label turnover, which may pose practical limitations in certain applications, particularly in patients or elderly population. It would be interesting to test whether using shorter metabolite time courses would result in similar metabolic rates, thereby significantly reducing scan times. Steady-state deuterium imaging could benefit from the excellent sensitivity and imaging resolution as achieved in this dynamic DMRSI study, and deuterated metabolite ratio, such as [Lac]/([Lac] + [Glx]), may provide alternative measures of aerobic versus oxidative glycolysis. However, the validity of such a qualitative marker and its relationship with the ratios of relevant metabolic rates need to be carefully evaluated. The kinetic model currently used may require further validation and/or improvement, as we did not account for a possible label loss during the glycolytic pathway (69). In addition, the blood input functions derived from measured total and labeled plasma glucose are needed for kinetic modeling, which brings additional burden to the routine application of this imaging technology. Moreover, by better removing the signal from lipid contamination,

Table 1. Summary of CMR_{Glc}, V_{TCA}, CMR_{Lac}, and T_{max} values for pure WM, pure GM, and whole-brain (WB) average obtained from five healthy subjects.

	CMR_{Glc} (μmol/g/min)			V_{TCA} (μmol/g/min)			CMR_{Lac} (μmol/g/min)			T_{max} (μmol/g/min)		
	Pure WM	Pure GM	WB	Pure WM	Pure GM	WB	Pure WM	Pure GM	WB	Pure WM	Pure GM	WB
Subject 1	0.17	0.45	0.29	0.33	0.71	0.50	0.13	0.13	0.13	0.89	1.50	1.17
Subject 2	0.22	0.60	0.38	0.58	0.99	0.75	0.12	0.19	0.15	0.81	2.19	1.39
Subject 3	0.19	0.44	0.30	0.58	0.83	0.69	0.09	0.12	0.10	0.93	2.08	1.42
Subject 4	0.21	0.37	0.28	0.54	0.69	0.61	0.10	0.12	0.11	0.83	1.42	1.08
Subject 5	0.18	0.48	0.29	0.28	0.74	0.44	0.16	0.18	0.17	0.96	1.72	1.24
Mean ±SD	0.19±0.02	0.47±0.08	0.31±0.04	0.46±0.15	0.79±0.12	0.60±0.13	0.12±0.03	0.15±0.03	0.13±0.03	0.88±0.06	1.78±0.34	1.26±0.14

the metabolic map of Lac content and metabolic rate of Lac production can be further improved.

In summary, we have demonstrated that utilizing advanced RF coil design and postprocessing methods, dynamic DMRSI with unprecedented sensitivity and spatiotemporal resolutions can be achieved on an FDA-approved 7 T clinical scanner, enabling reliable mapping of deuterated metabolites contents and dynamics, and quantification of glucose metabolic rates and transportation rates using a newly developed kinetic model. We are now able to map CMR_{Glc}, V_{TCA}, and CMR_{Lac}, as well as T_{max} simultaneously across the entire human brain, distinguish tissue-specific metabolic activities, and determine the relationship between these metabolic rates to delineate the contributions of oxidative and nonoxidative glucose metabolism in the human brain. Therefore, the quantitative dynamic DMRSI technology demonstrated herein should be highly valuable for studying glucose metabolism in healthy and diseased brains, especially for quantitatively imaging the Warburg Effect in brain tumors, and studying metabolic reprogramming in healthy brain and/or in other brain disorders, including stroke and neurodegeneration diseases.

Materials and methods
RF coil design, construction, and characterization
EM simulation

Using the Hexahedral Time Domain solver (CST Studio 2019), we simulated B_1^- maps of three loop coils with 6, 12, and 18 cm diameters loaded with a head-shaped phantom (filled with a 42% polyvinylpyrrolidone solution mimicking the human brain properties) at 45.6, 120, and 297 MHz, corresponding to the ^2H, ^{31}P, and ^1H operating frequencies at 7 T, respectively. We also simulated an eight-element quadrature-driving low-pass birdcage ^2H volume coil, and 4ch, 5ch, and 8ch ^2H head array coils with similar geometry but decreasing coil size to cover the same phantom. After full-wave simulation, we tuned and matched each channel of these coils to the ^2H operating frequency at 45.6 MHz, and combined the B_1^+ fields based on the circuit optimization mentioned in the previous publication (70). For all ^2H coils, we achieved optimal tuning and matching for each coil ($S_{11} < -20$ dB) and intercoil decoupling ($S_{12} < -15$ dB). Finally, we generated the combined RF transmission (B_1^+) and reception (B_1^-) magnetic fields for all ^2H array coils and the volume coil driven by 1-V forward voltage.

Design and construction of RF head array coil and interface

We designed and built a 4ch $^1H/^2H$ dual-frequency transceiver (Tx/Rx) head array coil to cover the entire human head, where large ^2H coils facing each other are decoupled using a modified RID circuits (60) elongated by coaxial cables at both ends. We achieved excellent coil decoupling ($S_{12} < -20$ dB) for all ^2H loop coils. For proton imaging, we added four large-sized ^1H loop coils as a 4ch ^1H Tx/Rx array coil on top of the 4ch ^2H Tx/Rx array coil. The overlap pattern between the ^1H and ^2H array layers is similar to the published work (71, 72), where the overlap of adjacent ^1H coil pairs is interleaved with the overlap of adjacent ^2H coil pairs (Fig. 1D) for achieving better decoupling between them. The 4ch-^1H and 4ch-^2H Tx/Rx head array coils were both driven in the single channel transmit mode (1Tx) by a ^1H RF amplifier and an X-nuclei RF amplifier, respectively, followed by a four-way power splitter and phase shifters. At the receiving end, both ^1H and ^2H head array coils were received in uncombined multichannel receive mode (4 × Rx). The ^1H and ^2H head array coils were connected to ^1H and ^2H T/R switches with a

built-in low input impedance amplifier (LNA) tuned to 297 and 45.6 MHz, respectively.

RF coil characterization

To generate B_1 field maps, we used the 3D-DMRSI datasets acquired with varied RF pulse voltages under the fully relaxed condition, and fitted the HDO deuterium signals in a given DMRSI voxel to the RF pulse voltage according to a "sine" function for determining the 90° FA voltage ($\propto 1/B_1^+$) and corresponding maximum HDO signal intensity (i.e. relative $B_1^- \propto$ SNR) (73).

Human participants and study procedures

Two groups of healthy volunteers from the local communities surrounding the University of Minnesota were recruited to participate in this study. The first group of participants (three females and five males, 43 ± 19 years old) were scanned without introducing any deuterium label for evaluation of 4ch-^{1}H/^{2}H RF head array coil performance and determine the ^{2}H coil sensitivity using the natural abundance brain tissue HDO signals. The second group (four females and four males, 38 ± 18 years old) participated in the dynamic DMRSI study with oral administration of D66 (Cambridge Isotope Lab, 0.75 g/kg, maximum dose 60 g, 30% solution); five of them (three females and two males) had their glucose blood input functions measured during the dynamic DMRSI scans; and two of them (one male and one female) were scanned repeatedly on two different days with interscan intervals of 45 and 100 days, respectively. The study was conducted in the morning, and all subjects participating in the dynamic DMRSI scan were asked to fast overnight before the imaging study. The general workflow of the study is depicted in Fig. 4A; brain structural images and baseline DMRSI data were collected before D66 administration. Subjects drank the D66 solution through a flexible straw while having their head in the same position within the RF head array coil. Dynamic DMRSI acquisition began after the patient table returned to the same position inside the magnet.

When needed, multiple arterialized venous blood samples (about 2 cc per sample, up to 12 samples per scan session) were collected from the subjects' ankles during the dynamic DMRSI scan (74). Total blood glucose and deuterated plasma glucose levels in each blood sample were measured using glucometer (Germaine Laboratories, Inc., San Antonio, TX, USA) and HR NMR instrument (Bruker Avance III 500 MHz), respectively (1), to derive relevant blood input functions for kinetic modeling (Fig. 4A). The Institutional Review Board of the University of Minnesota approved all study procedures involving human participants. Informed consent was obtained from all participants.

MRI system and data acquisition

All MRI measurements were performed on the standard Siemens actively shielded 7 T/90 cm bore MAGNETOM or 7 T/ 84 cm bore TERRA human scanner with an additional ^{2}H

imaging option to enable deuterium MRS imaging and data acquisition.

Human brian structure imaging

The anatomical information of each subject was collected for co-registration with the deuterium imaging and tissue segmentation. We acquired MPRAGE proton density (PD) and T_1w images with 1 mm isotropic resolution and generated brain structural images via dividing T_1w by the PD image. Our FSL-based (75) postprocessing pipeline includes noise reduction, brain extractions, and brain tissue segmentations into GM, WM, and cerebrospinal fluid (CSF). After co-registration with the DMRSI data, the segmented structural images were down sampled to match the DMRSI resolution, and the tissue fractions of GM, WM, and CSF (F_{GM}, F_{WM}, and F_{CSF}) were calculated for all DMRSI voxels within the brain. To calculate the tissue water fractions in each voxel, we assumed 0.71, 0.83, and 1.0 water fraction of WM, GM, and CSF, respectively, based on the literature report (76) and generated a water fraction map using the following equation:

$$\text{Voxel}_{\text{WaterFraction}} = 0.71 \times F_{WM} + 0.83 \times F_{GM} + F_{CSF}.$$

Dynamic DMRSI acquisition

We used the 4ch ^{2}H/^{1}H dual-frequency head array coil (Fig. 1D and E) to acquire whole-brain HR-DMRSI data based on the Fourier Series Weighted 3D-CSI sequence (77) in healthy subjects before and after the D66 oral intake with following acquisition parameters: field of view of $18 \times 18 \times 15$ or $20 \times 20 \times 15$ cm^3 depending on individual head size; matrix size of $19 \times 19 \times 15$, spectral bandwidth of 1,200 Hz, 180 number of FID points, repetition time (TR) of 173 ms, nominal RF pulse FA of 56° and 2.5 min total scan time per CSI volume; cylindrical-shaped voxel and nominal voxel size of 0.7 cc (for most subjects) or 0.9 cc.

Imaging reconstruction

See details of methods for combining the DMRSI signals from multiple Rx channels and for SPICE processing in the Supplementary Material.

Novel approaches for concentration and metabolic rates quantification

Metabolite concentration quantification

For each human study, we collected 10 min (4 volumes) baseline DMRSI data, followed by at least 90 min (36 volumes) of dynamic DMRSI data after oral administration of D66 glucose. To correct inhomogeneous B_1^+ field of the ^{2}H head array coil, i.e. varied RF pulse FA ($\propto B_1^+$) and saturation effect in space, we obtained the ^{2}H FA maps using the brain HDO signals in two DMRSI datasets acquired at the end of each study with the following equation:

$$FA = \cos^{-1}\left(\frac{\sqrt{1 - 2\left[\left(\frac{M_{2s}}{M_s}\right)\exp\left(-\frac{TR}{T_1}\right) - \exp\left(-\frac{TR}{T_1}\right)\right] \times \left[-\left(\frac{M_{2s}}{M_s}\right) - \left(\frac{M_{2s}}{M_s}\right)\exp\left(-\frac{TR}{T_1}\right)\right] - 1}}{2\left[\left(\frac{M_{2s}}{M_s}\right)\exp\left(-\frac{TR}{T_1}\right) - \exp\left(-\frac{TR}{T_1}\right)\right]}\right)$$

where M_s and M_{2s} are the two measurements using the same TR of 173 ms ($<<5 \times T_1$) and FA of α and 2α, respectively. The SFs based on the FA maps and T_1 (longitudinal relaxation time) values of Glx, Glc, Lac, and HDO at 7 T (59) can be calculated using the following equation:

$$SF = \frac{1 - e^{-TR/T_1}}{1 - \cos(FA) \times e^{-TR/T_1}}.$$

To quantify the molar concentration of deuterated metabolites, the baseline HDO signal ($S_{\text{Base HDO}}$) was used as the internal reference to normalize the ^{2}H signals of each metabolite. Since the ^{2}H concentration in natural abundance (pure) water is 17.16 mM (1), by multiplying this concentration to the brain water fraction in each DMRSI voxel (Voxel$_{\text{WaterFraction}}$), we can derive the molar concentration maps of different deuterated metabolites. These concentration values were corrected by the number of ^{2}H atoms in each molecule; therefore, the concentrations of the deuterated HDO, Glc, Glx, and Lac in each DMRSI voxel and at each post-D66 time point were calculated according to the following equations:

$$[HDO] = \frac{S_{\text{D66 HDO}}}{S_{\text{Base HDO}}} \times \frac{17.16}{1} \times \text{Voxel}_{\text{WaterFraction}}$$

$$[Glc] = \frac{S_{\text{Glc}}}{SF_{\text{Glc}}} \times \frac{SF_{\text{HDO}}}{S_{\text{Base HDO}}} \times \frac{17.16}{2} \times \text{Voxel}_{\text{WaterFraction}}$$

$$[Glx] = \frac{S_{\text{Glx}}}{SF_{\text{Glx}}} \times \frac{SF_{\text{HDO}}}{S_{\text{Base HDO}}} \times \frac{17.16}{1.33} \times \text{Voxel}_{\text{WaterFraction}}$$

$$[Lac] = \frac{S_{\text{Lac}}}{SF_{\text{Lac}}} \times \frac{SF_{\text{HDO}}}{S_{\text{Base HDO}}} \times \frac{17.16}{2} \times \text{Voxel}_{\text{WaterFraction}}$$

where $S_{\text{D66 HDO}}$, S_{Glc}, S_{Glx}, and S_{Lac} are the HDO, Glc, Glx, and Lac signal after the D66 oral administration; and SF_{HDO}, SF_{Glc}, SF_{Glx}, and SF_{Lac} are the SF of HDO, Glc, Glx, and Lac.

Figure S3A shows representative brain slices and corresponding SF and brain water fraction maps used to quantify the molar concentration of Glc, Glx, Lac, and HDO, before (Fig S3B) and after (Fig. S3C) correcting the effects of SF and brain water fraction in the quantification.

Metabolic rate quantification with kinetic modeling

The values of CMR$_{\text{Glc}}$, CMR$_{\text{Lac}}$, V_{TCA}, and T_{max} were quantified using the time courses of deuterated metabolite concentrations, the glucose blood input functions and the kinetic model (Fig. 4B) modified from previous animal study (1); and the following model parameters: [Glc]$_{\text{brain}}$ = 1.2 mM, [Pyruvate]$_{\text{brain}}$ = 0.17 mM, [Lac]$_{\text{brain}}$ = 1 mM, [α-ketoglutarate]$_{\text{brain}}$ = 0.12 mM, [Glx]$_{\text{brain}}$ = 15 mM, V_{out} = 0.1 mM/min, K_T = 15 mM/min, V_x = 30 mM/min. V_{out} presents the net flux of Lac between the brain tissue and blood pool, K_T is the half-saturation constant for both forward and reverse glucose transport, and T_{max} is the maximum apparent rate of forward glucose transport based on the reversible Michaelis–Menten kinetic model (1, 78), which was determined in the model fitting. We quantified the deuterated plasma Glc (Glc*) and total blood Glc concentrations in multiple arterialized venous blood samples, and used their time courses as the blood input functions for the kinetic modeling. We then obtained the concentration time courses of the cerebral Glc, Glx, and Lac by solving the differential equations of the kinetic model using the MATLAB (MathWorks) ODE solver. The output dynamics of time

courses from the kinetic model were then fitted with the measured cerebral Glc, Glx, and Lac dynamics using the MATLAB least square curve fitting solver. After obtaining the metabolic rate maps through the kinetic modeling, we interpolated the low-resolution metabolic rate maps onto the HR maps for display, as shown in Figs. 5 and S8.

Statistical analysis

The DMRSI images and nonimage data were analyzed in MATLAB using custom scripts. The linear regression between the metabolic concentrations and GM fractions, between different metabolic rates, or between different experiments, was performed using the generalized linear models from MATLAB function (fitglm). All linear regression fits with $P < 0.005$ based on the t test were considered statistically significant.

Supplementary Material

Supplementary material is available at *PNAS Nexus* online.

Author Contributions

X.-H.Z. and W.C. designed the study. X.L. performed all the EM simulations and manufactured 4ch ^{1}H/^{2}H head array coil. X.L., X.-H.Z. and H.M.W. performed the DMRSI human experiments. X.L. and Y.L. processed the raw data. Y.L. and Z.-P.L. developed the SPICE-processing pipeline. X.L., X.-H.Z., and W.C. analyzed and interpreted the data. X.-H.Z. and T.W. measured the blood input functions. X.L., G.Z., X.-H.Z., and W.C. developed the kinetic model. X.L., X.-H.Z. and W.C. wrote the manuscript.

Data Availability

We have made the data and code for this work publicly available on github, and it is accessible *via* a persistent identifier. DOI: 10.5281/zenodo.14983911.

References

1 Lu M, Zhu XH, Zhang Y, Mateescu G, Chen W. 2017. Quantitative assessment of brain glucose metabolic rates using in vivo deuterium magnetic resonance spectroscopy. *J Cereb Blood Flow Metab.* 37:3518–3530.

2 Barinaga M. 1997. What makes brain neurons run? *Science.* 276: 196–198.

3 Magistretti PJ, Pellerin L, Rothman DL, Shulman RG. 1999. Energy on demand. *Science.* 283:496–497.

4 Mergenthaler P, Lindauer U, Dienel GA, Meisel A. 2013. Sugar for the brain: the role of glucose in physiological and pathological brain function. *Trends Neurosci.* 36:587–597.

5   Raichle ME. 2006. Neuroscience. The brain's dark energy. *Science.* 314:1249–1250.

6   Clarke DD, Sokoloff L. Circulation and energy metabolism of the brain. In: Siegel GJ, editor. *Basic neruochemistry: molecular, cellular and medical aspects.* Lippincott-Raven Publishers, Philadephia, 1999. p. 633–669.

7   Siesjo BK. *Brain energy metabolism.* Wiley, New York, 1978.

8   Faubert B, Solmonson A, DeBerardinis RJ. 2020. Metabolic reprogramming and cancer progression. *Science.* 368:eaaw5473.

9   Vander Heiden MG, Cantley LC, Thompson CB. 2009. Understanding the Warburg effect: the metabolic requirements of cell proliferation. *Science.* 324:1029–1033.

10 Warburg O. 1956. On the origin of cancer cells. *Science.* 123:309–314.

11 Ward PS, Thompson CB. 2012. Metabolic reprogramming: a cancer hallmark even Warburg did not anticipate. *Cancer Cell.* 21:297–308.

12 Fox PT, Raichle ME, Mintun MA, Dence C. 1988. Nonoxidative glucose consumption during focal physiologic neural activity. *Science.* 241:462–464.

13 Magistretti PJ. 2016. Imaging brain aerobic glycolysis as a marker of synaptic plasticity. *Proc Natl Acad Sci U S A.* 113:7015–7016.

14 Prichard J, et al. 1991. Lactate rise detected by ^{1}H NMR in human visual cortex during physiologic stimulation. *Proc Natl Acad Sci U S A.* 88:5829–5831.

15 Shannon BJ, et al. 2016. Brain aerobic glycolysis and motor adaptation learning. *Proc Natl Acad Sci U S A.* 113:E3782–E3791.

16 Vaishnavi SN, et al. 2010. Regional aerobic glycolysis in the human brain. *Proc Natl Acad Sci U S A.* 107:17757–17762.

17 Goyal MS, et al. 2017. Loss of brain aerobic glycolysis in normal human aging. *Cell Metab.* 26:353–360.e3.

18 Goyal MS, et al. 2023. Brain aerobic glycolysis and resilience in Alzheimer disease. *Proc Natl Acad Sci U S A.* 120:e2212256120.

19 Murai T, Matsuda S. 2023. Metabolic reprogramming toward aerobic glycolysis and the gut microbiota involved in the brain amyloid pathology. *Biology (Basel).* 12:1081.

20 Rebelos E, Rinne JO, Nuutila P, Ekblad LL. 2021. Brain glucose metabolism in health, obesity, and cognitive decline-does insulin have anything to do with it? A narrative review. *J Clin Med.* 10:1532.

21 Vlassenko AG, Raichle ME. 2015. Brain aerobic glycolysis functions and Alzheimer's disease. *Clin Transl Imaging.* 3:27–37.

22 Ardenkjaer-Larsen JH, et al. 2003. Increase in signal-to-noise ratio of > 10,000 times in liquid-state NMR. *Proc Natl Acad Sci U S A.* 100:10158–10163.

23 Grist JT, et al. 2020. Hyperpolarized ^{13}C MRI: a novel approach for probing cerebral metabolism in health and neurological disease. *J Cereb Blood Flow Metab.* 40:1137–1147.

24 Huang SC, et al. 1980. Noninvasive determination of local cerebral metabolic rate of glucose in man. *Am J Physiol.* 238:E69–E82.

25 Phelps ME, et al. 1979. Tomographic measurement of local cerebral glucose metabolic rate in humans with (F-18)2-fluoro-2-deoxy-D-glucose: validation of method. *Ann Neurol.* 6:371–388.

26 Reivich M, et al. 1979. The [^{18}F]fluorodeoxyglucose method for the measurement of local cerebral glucose utilization in man. *Circ Res.* 44:127–137.

27 Wang ZJ, et al. 2019. Hyperpolarized ^{13}C MRI: state of the art and future directions. *Radiology.* 291:273–284.

28 de Graaf RA, Mason GF, Patel AB, Behar KL, Rothman DL. 2003. In vivo ^{1}H-[^{13}C]-NMR spectroscopy of cerebral metabolism. *NMR Biomed.* 16:339–357.

29 Morris P, Bachelard H. 2003. Reflections on the application of 13C-MRS to research on brain metabolism. *NMR Biomed.* 16:303–312.

30 Martin WR, Powers WJ, Raichle ME. 1987. Cerebral blood volume measured with inhaled C^{15}O and positron emission tomography. *J Cereb Blood Flow Metab.* 7:421–426.

31 Mintun MA, Raichle ME, Martin WR, Herscovitch P. 1984. Brain oxygen utilization measured with O-15 radiotracers and positron emission tomography. *J Nucl Med.* 25:177–187.

32 Raichle ME, Martin WR, Herscovitch P, Mintun MA, Markham J. 1983. Brain blood flow measured with intravenous H$_2^{15}$O. II. Implementation and validation. *J Nucl Med.* 24:790–798.

33 Lu M, Zhu XH, Zhang Y, Low W, Chen W. Simultaneous assessment of abnormal glycolysis and oxidative metabolisms in brain tumor using in vivo deuterium ^{2}H MRS imaging. *Proc Intl Soc Mag Reson Med.* 24:3962. 2016.

34 Ruhm L, et al. 2021. Deuterium metabolic imaging in the human brain at 9.4 Tesla with high spatial and temporal resolution. *Neuroimage.* 244:118639.

35 Lu M, Zhu XH, Yi Z, Mateescu G, Chen W. Quantitative assessment of glucose metabolism in rat brains using in vivo deuterium magnetic resonance. *Proc Intl Soc Mag Reson Med.* 22:0537. 2014.

36 Simoes RV, et al. 2022. Glucose fluxes in glycolytic and oxidative pathways detected in vivo by deuterium magnetic resonance spectroscopy reflect proliferation in mouse glioblastoma. *Neuroimage Clin.* 33:102932.

37 Ackerman JJ, Grove TH, Wong GG, Gadian DG, Radda GK. 1980. Mapping of metabolites in whole animals by ^{31}P NMR using surface coils. *Nature.* 283:167–170.

38 Hayes CE, Roemer PB. 1990. Noise correlations in data simultaneously acquired from multiple surface coil arrays. *Magn Reson Med.* 16:181–191.

39 Lam F, Liang ZP. 2014. A subspace approach to high-resolution spectroscopic imaging. *Magn Reson Med.* 71:1349–1357.

40 Li Y, et al. 2021. Machine learning-enabled high-resolution dynamic deuterium MR spectroscopic imaging. *IEEE Trans Med Imaging.* 40:3879–3890.

41 Nguyen HM, Peng X, Do MN, Liang ZP. 2013. Denoising MR spectroscopic imaging data with low-rank approximations. *IEEE Trans Biomed Eng.* 60:78–89.

42 Yu Y, Herman P, Rothman DL, Agarwal D, Hyder F. 2018. Evaluating the gray and white matter energy budgets of human brain function. *J Cereb Blood Flow Metab.* 38:1339–1353.

43 de Graaf RA, et al. 2001. Differentiation of glucose transport in human brain gray and white matter. *J Cereb Blood Flow Metab.* 21:483–492.

44 Huisman MC, et al. 2012. Cerebral blood flow and glucose metabolism in healthy volunteers measured using a high-resolution PET scanner. *EJNMMI Res.* 2:63.

45 Hyder F, et al. 2016. Uniform distributions of glucose oxidation and oxygen extraction in gray matter of normal human brain: no evidence of regional differences of aerobic glycolysis. *J Cereb Blood Flow Metab.* 36:903–916.

46 Chen Ming Low J, Wright AJ, Hesse F, Cao J, Brindle KM. 2023. Metabolic imaging with deuterium labeled substrates. *Prog Nucl Magn Reson Spectrosc.* 134–135:39–51.

47 De Feyter HM, de Graaf RA. 2021. Deuterium metabolic imaging—back to the future. *J Magn Reson.* 326:106932.

48 Ouwerkerk R. 2020. Deuterium MR spectroscopy: a new way to image glycolytic flux rates. *Radiology.* 294:297–298.

49 Pan F, et al. 2024. Advances and prospects in deuterium metabolic imaging (DMI): a systematic review of in vivo studies. *Eur Radiol Exp.* 8:65.

50 Zhu XH, Lu M, Chen W. 2018. Quantitative imaging of brain energy metabolisms and neuroenergetics using in vivo X-nuclear ^{2}H, ^{17}O and ^{31}P MRS at ultra-high field. *J Magn Reson.* 292:155–170.

51 De Feyter HM, *et al.* 2018. Deuterium metabolic imaging (DMI) for MRI-based 3D mapping of metabolism in vivo. *Sci Adv.* 4:eaat7314.

52 Hesse F, *et al.* 2021. Monitoring tumor cell death in murine tumor models using deuterium magnetic resonance spectroscopy and spectroscopic imaging. *Proc Natl Acad Sci U S A.* 118:e2014631118.

53 Ip KL, Thomas MA, Behar KL, de Graaf RA, De Feyter HM. 2023. Mapping of exogenous choline uptake and metabolism in rat glioblastoma using deuterium metabolic imaging (DMI). *Front Cell Neurosci.* 17:1130816.

54 Kreis F, *et al.* 2020. Measuring tumor glycolytic flux in vivo by using fast deuterium MRI. *Radiology.* 294:289–296.

55 Lu M, Zhu XH, Zhang Y, Low W, Chen W, *et al.* High-resolution deuterium MR spectroscopic imaging of the Warburg effect in brain tumor. *Proc Intl Soc Mag Reson Med.* 26:4852. 2018.

56 Montrazi ET, *et al.* 2023. High-sensitivity deuterium metabolic MRI differentiates acute pancreatitis from pancreatic cancers in murine models. *Sci Rep.* 13:19998.

57 Veltien A, *et al.* 2021. Simultaneous recording of the uptake and conversion of glucose and choline in tumors by deuterium metabolic imaging. *Cancers (Basel).* 13:4034.

58 Song KH, *et al.* 2024. Deuterium magnetic resonance spectroscopy quantifies tumor fraction in a mouse model of a mixed radiation necrosis/GL261-glioblastoma lesion. *Mol Imaging Biol.* 26:173–178.

59 Roig ES, *et al.* 2022. Deuterium metabolic imaging of the human brain in vivo at 7 T. *Magn Reson Med.* 89:29–39. https://doi.org/10.1002/mrm.29439

60 Avdievich NI, Pan JW, Hetherington HP. 2013. Resonant inductive decoupling (RID) for transceiver arrays to compensate for both reactive and resistive components of the mutual impedance. *NMR Biomed.* 26:1547–1554.

61 Li X, *et al.* A multinuclear 4-channel ^{2}H loop and 4-channel ^{1}H microstrip array coil for human head MRS/MRI at 7T. *Proc Intl Soc Mag Reson Med.* 30:4510 2022.

62 Zhu XH, *et al.* 2021. Quantitative assessment of occipital metabolic and energetic changes in Parkinson's patients, using *in vivo* ^{31}P MRS-based metabolic imaging at 7T. *Metabolites.* 11:145.

63 Pan JW, *et al.* 2000. Spectroscopic imaging of glutamate C4 turnover in human brain. *Magn Reson Med.* 44:673–679.

64 Shulman RG, Rothman DL, Behar KL, Hyder F. 2004. Energetic basis of brain activity: implications for neuroimaging. *Trends Neurosci.* 27:489–495.

65 Zhu XH, *et al.* 2012. Quantitative imaging of energy expenditure in human brain. *Neuroimage.* 60:2107–2117.

66 de Graaf RA, *et al.* 2020. On the magnetic field dependence of deuterium metabolic imaging. *NMR Biomed.* 33:e4235.

67 Adamson PM, *et al.* 2024. Deuterium metabolic imaging for 3D mapping of glucose metabolism in humans with central nervous system lesions at 3T. *Magn Reson Med.* 91:39–50.

68 Khan AS, *et al.* 2024. Deuterium metabolic imaging of Alzheimer disease at 3-T magnetic field strength: a pilot case-control study. *Radiology.* 312:e232407.

69 de Graaf RA, Thomas MA, Behar KL, De Feyter HM. 2021. Characterization of kinetic isotope effects and label loss in deuterium-based isotopic labeling studies. *ACS Chem Neurosci.* 12:234–243.

70 Li X, Pan JW, Avdievich NI, Hetherington HP, Rispoli JV. 2021. Electromagnetic simulation of a 16-channel head transceiver at 7 T using circuit-spatial optimization. *Magn Reson Med.* 85:3463–3478.

71 Avdievich NI, *et al.* 2020. Double-tuned ^{31}P/^{1}H human head array with high performance at both frequencies for spectroscopic imaging at 9.4T. *Magn Reson Med.* 84:1076–1089.

72 Wang B, *et al.* 2021. A radially interleaved sodium and proton coil array for brain MRI at 7 T. *NMR Biomed.* 34:e4608.

73 Lee BY, *et al.* 2017. Large improvement of RF transmission efficiency and reception sensitivity for human in vivo ^{31}P MRS imaging using ultrahigh dielectric constant materials at 7T. *Magn Reson Imaging.* 42:158–163.

74 Seaquist ER. 1997. Comparison of arterialized venous sampling from the hand and foot in the assessment of in vivo glucose metabolism. *Metabolism.* 46:1364–1366.

75 Jenkinson M, Beckmann CF, Behrens TEJ, Woolrich MW, Smith SM. 2012. FSL. *Neuroimage.* 62:782–790.

76 Whittall KP, *et al.* 1997. In vivo measurement of T_2 distributions and water contents in normal human brain. *Magn Reson Med.* 37:34–43.

77 Hendrich K, *et al.* 1994. Spectroscopic imaging of circular voxels with a two-dimensional Fourier-series window technique. *J Magn Reson B.* 105:225–232.

78 Gruetter R, Ugurbil K, Seaquist ER. 1998. Steady-state cerebral glucose concentrations and transport in the human brain. *J Neurochem.* 70:397–408.